frontiers in Materials

ORIGINAL RESEARCH
published: 05 February 2021
doi: 10.3389/fmats.2020.640081

Characteristics of Passive Films Formed on As-Cast Ti–6Al-4V in Hank's Solution Before and After Transpassivation

Guo Yi[1], Xinxin Liu[2], Chuanbo Zheng[1,3], Hongyue Zhang[1], Cheng Xu[1], Yu-Wei Cui[2] and Shuan Liu[3]*

[1]School of Materials Science and Engineering, Jiangsu University of Science and Technology, Zhenjiang, China, [2]School of Science, Jiangsu University of Science and Technology, Zhenjiang, China, [3]Key Laboratory of Marine Materials and Related Technologies, Zhejiang Key Laboratory of Marine Materials and Protective Technologies, Ningbo Institute of Materials Technologies and Engineering, Chinese Academy of Sciences, Ningbo, China

In this work, the characteristics of passive films formed on as-cast Ti-6Al-4V before and after transpassivation by electrochemical methods will be studied. A simulated body fluid of Hank's solution was used as the electrolyte in this work. According to the potentiodynamic polarization test, the passivation range, transpassive range, and repassivation range of as-cast Ti-6Al-4V were obtained. Afterward, the potentiostatic polarization was employed to passivate the Ti-6Al-4V in both passivation and repassivation ranges. Electrochemical impedance spectroscopy (EIS) was used to analyze the characteristics of formed passive films. Different electrochemical behavior of as-cast Ti–6Al-4V is found in passivation and repassivation ranges. The passivation current density of the sample in the repassivation range is significantly larger than that in the passivation range. Meanwhile, the growth rate of passive film in the repassivation range is also greater than that in the passivation range. Although the sample shows a higher charge transfer impedance in the repassivation range, metastable pitting corrosion is also observed, indicating the formation of the unstable passive film. Such results advance the understanding of as-cast Ti-6Al-4V polarized under different potentials for potential biomedical applications.

Keywords: Ti-6Al-4V, corrosion, passive film, transpassivation, electrochemical measurement, Mott-Schottky

OPEN ACCESS

Edited by:
Liqiang Wang,
Shanghai Jiao Tong University, China

Reviewed by:
Jun Cheng,
Northwest Institute For Non-Ferrous Metal Research, China
Linjiang Chai,
Chongqing University of Technology, China

****Correspondence:***
Chuanbo Zheng
15952802516@139.com

Specialty section:
This article was submitted to Biomaterials, a section of the journal Frontiers in Materials.

Received: *10 December 2020*
Accepted: *23 December 2020*
Published: *05 February 2021*

Citation:
Yi G, Liu X, Zheng C, Zhang H, Xu C, Cui Y-W and Liu S (2021) Characteristics of Passive Films Formed on As-Cast Ti–6Al-4V in Hank's Solution Before and After Transpassivation. Front. Mater. 7:640081. doi: 10.3389/fmats.2020.640081

INTRODUCTION

Titanium (Ti) and its alloys are widely used in a wide variety of industrial applications, such as biomedical, marine, and chemical industries, due to their fascinating properties, including high specific strength, excellent corrosion resistance, and good biocompatibility (Lu et al., 2009; Rabadia et al., 2019a; Zhang and Chen, 2019; Chen et al., 2020a; Liu et al., 2020). Primarily, Ti alloys can be classified as α-type Ti alloys (Zhang and Attar, 2016; Chen et al., 2017b; Zheng et al., 2019; Chen et al., 2020b), (α+β)-type Ti alloys (Kang and Yang, 2019; Montiel et al., 2020; Semenova et al., 2020), β-type Ti alloys (Zhang et al., 2011; Wang et al., 2016; Wang et al., 2018a; Rabadia et al., 2019b; S. Liu et al., 2020), and Ti-based composites (Zhang and Xu, 2004; Zhang et al., 2006; Lu et al., 2009; Yang et al., 2020a; Yang et al., 2020b). Among the commercial Ti materials, Ti–6Al–4V alloy has received considerable attention owing to good fatigue resistance, strength, and corrosion resistance (Bai et al., 2017; Dai et al., 2017; Zhao et al., 2018). However, Ti–6Al–4V still has some intrinsic disadvantages.

For example, Ti–6Al–4V exhibits a relatively low hardness of 290–375 HV (Zhang et al., 2020b). The low wear resistance of Ti–6Al–4V may easily cause the seizure in service (Stolyarov et al., 2004). Furthermore, although Ti–6Al–4V exhibits good corrosion resistance in the corrosive environment, a complex corrosive environment always degrades the corrosion resistance of Ti–6Al–4V due to the presence of halogen ions, hydrogen ions, hydroxyl ions, and also other functional groups (Hanawa, 2004; Chen and Thouas, 2015; Yu et al., 2015; Qin et al., 2019). Such species degrade the passive film formed on Ti–6Al–4V and thereby the corrosion resistance. Therefore, surface modifications are frequently employed to produce the barrier layer on Ti–6Al–4V before it is applicated.

So far, there are a variety of surface modification methods for improving the surface properties of metallic materials, such as laser processing (Balla et al., 2010; Chai et al., 2017; Chai et al., 2018; Xiang et al., 2020), microarc oxidation (Wang et al., 2018b; Dehghanghadikolaei et al., 2019; Yang et al., 2020b), thermal spraying (Jaeggi et al., 2011; Chen et al., 2019a; Chen et al., 2019b), friction stir processing (Wang et al., 2015; Wang et al., 2017; Zhang et al., 2019c), ion implantation (Rautray et al., 2011; Qin et al., 2017), and so on. Among these methods, anodic oxidation is a costly method that applies an anodic potential on the metallic sample in the solution. Afterward, a compact and protective oxide film can be produced after the anodic oxidation process (Liu et al., 2004). Such a protective oxide film enhances the surface properties of Ti and Ti alloys. Therefore, anodic oxidation is a good method to synthesize different types of oxide films on metallic materials. The primary advantage of anodic oxidation is the good adhesion and bonding between the oxide film and Ti substrate. Hence, the anodic oxidized Ti and Ti alloys can be well-employed in the aerospace and biomedical industry (Aladjem, 1973; Babilas et al., 2016; Yang et al., 2020c).

The thickness of the produced oxide film on Ti and Ti alloys is determined by the applied anodic potential (Liu et al., 2004). Generally, the thickness of oxide film is almost linearly dependent on the applied potential, obeying the relationship of $d = \alpha U$, where d is the thickness of produced oxide film and U is the applied potential. α is a constant, which is within a range of 1.5–3 nm V^{-1}, depending on the chemical compositions of Ti electrodes and solution (Liu et al., 2004). However, such an empirical formula may be not accurate since the transpassive behavior and the repassivation are always found in the potentiodynamic polarization curve of Ti and Ti alloys above the applied potential of about 1–1.5 V (Narayanan and Seshadri, 2008; Qin et al., 2019; Seo and Lee, 2019). The transpassive behavior of Ti and Ti alloys results from the oxygen evolution reaction (Kong and Wu, 2007). Water is decomposed into H_2 and O_2 during this reaction, leading to the imperfection of the passive films formed on Ti and Ti alloys. Therefore, is this equation appropriate for Ti and Ti alloys in all passivation range? Or is the passivation film produced at the higher potential certainly better than that produced at lower potential? Such questions are still unclear. However, the information regarding the passive films produced before and after transpassive behavior is significantly important to the further understanding of the passivation behavior of Ti and Ti alloys and their wider applications.

Therefore, in this work, as-cast Ti–6Al–4V is selected as the experimental alloy. According to the potentiodynamic polarization curve, the first passivation range and the repassivation range can be obtained. Subsequently, the oxide films are produced at the different passivation range and are investigated based on their semiconductive properties and impedances. Hence, electrochemical measurements are primarily used and the formation mechanism of oxide film on Ti–6Al–4V.

EXPERIMENTAL

Material Preparation and Microstructural Characterization

As-cast Ti–6Al–4V alloy was prepared via vacuum arc remelting three times to ensure uniformity. The compositions of the experimental alloy were 5.94 wt% Al, 4.28 wt% V, and the balance of Ti. The sample was ground and polished to a mirror surface finish. Afterward, the polished sample was etched in a mixed solution of HF, HNO_3, and H_2O for about 15 s (1:2:7 in vol%). The microstructure of the etched sample was examined by an optical microscope (OM, OLYMPUS PMG3). The phase constituent of the polished sample was analyzed by an X-ray diffraction (XRD) diffractometer (Empyrean, PANalytical) with Co-K_α radiation. During the XRD test, the following parameters were used: the scanning range was between 30° and 100°, and the scanning rate was 0.03°/s. Jade 6.5 software was used to analyze the obtained XRD data.

Electrochemical Measurements

The specimens with a size of 10 × 10 × 10 mm^3 were employed for electrochemical measurements. The exposure area of the specimen was about 100 mm^2. Hank's solution is used as the electrolyte and composed of 0.35 g/L $NaHCO_3$, 0.140 gL^{-1} $CaCl_2$, 0.098 gL^{-1} $MgSO_4$, 0.4 gL^{-1} KCl, 0.06 gL^{-1} KH_2PO_4, 8 gL^{-1} NaCl, 0.048 gL^{-1} Na_2HPO_4, 1 gL^{-1} $C_6H_{12}O_6$, and 0.011 gL^{-1} $C_{19}H_{14}O_5SNa$. The pH of Hank's solution is adjusted to 7.35 by diluted HCl and NaOH. A three-electrode-system electrochemical workstation (CHI660E, Chenhua) was employed for characterizing the corrosion behavior of as-cast Ti-6Al-4V. Ti-6Al-4V was employed as the working electrode, a platinum sheet was used as the counter electrode, and a saturated calomel electrode (SCE) was used as the reference electrode. The open-circuit potential (OCP) test for 1800 s was conducted before the electrochemical impedance spectroscopy (EIS) test and potentiodynamic polarization test. Subsequently, a potentiodynamic polarization test was conducted in a sweeping range of −0.25–+2 V (vs. OCP) at a sweeping step of 0.2 mV/s. According to the potentiodynamic polarization test, the passivation range, transpassive range, and repassivation range were obtained. Therefore, the potentiostatic polarization was employed to passivate the Ti-6Al-4V samples at the potentials of 0.1 V_{SCE}, 0.3 V_{SCE}, 0.5 V_{SCE}, 0.7 V_{SCE}, 0.9 V_{SCE}, 2.1 V_{SCE}, 2.3 V_{SCE}, 2.5 V_{SCE}, 2.7 V_{SCE}, and 2.9 V_{SCE}. Then, EIS was conducted to acquire effective capacitance at 1 kHz (Guan et al., 2018). Subsequently, Mott-Schottky tests were done at the frequency of 1 kHz, sweeping the potential from film formation potential to −

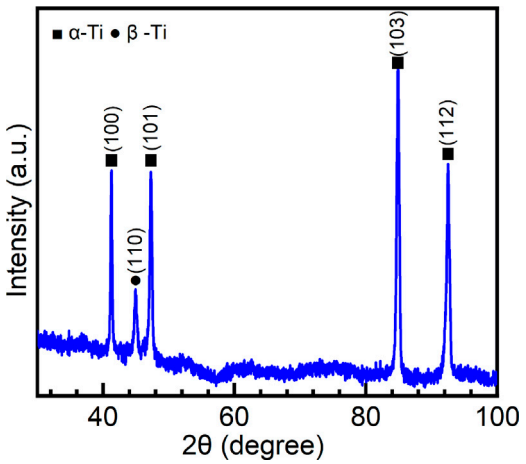

FIGURE 1 | X-ray diffraction pattern of as-cast Ti-6Al-4V used in this work.

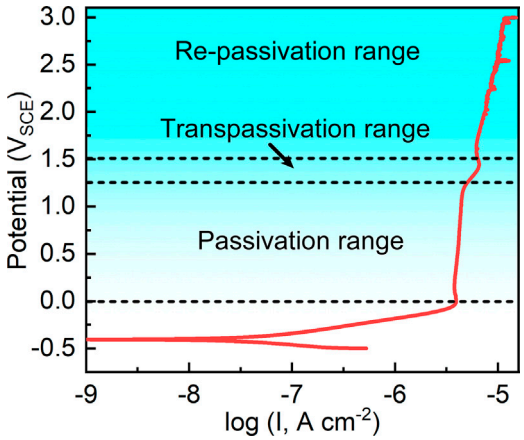

FIGURE 3 | Potentiodynamic polarization curve of as-cast Ti-6Al-4V in Hank's solution at 37°C.

1.0 V (vs. OCP) with a step of 10 mV/s. All potentials reported were against SCE in this work. Each test was repeated three times to ensure the data reproducibility. The software ZsimpWin 3.30 was used to analyze the EIS data and the software Cview 2.6 was used to analyze the potentiodynamic polarization data.

RESULTS AND DISCUSSION

Microstructural Features

Figure 1 shows the XRD pattern of the Ti-6Al-4V sample. Since Ti-6Al-4V is a dual-phase Ti alloy ((α+β)-type Ti alloy), the peaks of both α-Ti and β-Ti are observed. V is a β-stabilizer for Ti alloys (Chen et al., 2020a). Due to the small content of V in the sample, only a weak peak of β-Ti is observed in the XRD pattern. According to the integrated area method (Zhang et al., 2003;Chen et al., 2018a; Sang et al., 2019), the volume fraction of α-Ti is calculated to be 95% and β-Ti is 5%. Generally, (α+β)-type Ti alloys contain a certain fraction of β phase (about 5–30 vol%) (Lei et al., 2017). Therefore, (α+β)-type Ti alloys are heat treatable due to the second phase in the metal matrix (Chen et al., 2015b; Zhang et al., 2017; Sabban et al., 2019). **Figure 2** is the optical image of the microstructure of Ti-6Al-4V. It can be observed that the primary β grains have a size over several hundred microns. β-Ti is distributed on the boundaries of primary β grains. In the inner part of primary β grains, a considerable number of α-Ti laths are found. Such a Widmanstätten microstructure is produced due to the transformation of β → α at a relatively low speed. Similar microstructures can be frequently found in the hexagonal close-packed metallic materials, such as Zr alloys and other Ti alloys (Chen et al., 2018b; Chen et al., 2018c; Yang et al., 2019; Yang et al., 2020a).

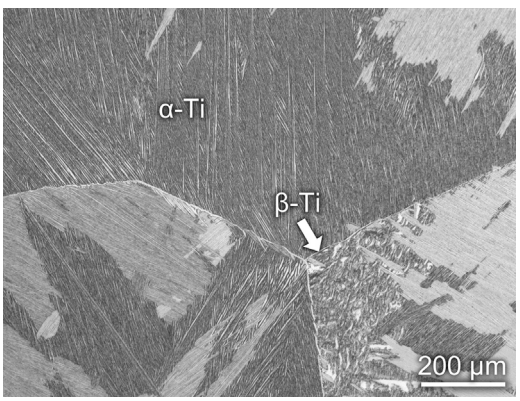

FIGURE 2 | Optical image of the microstructure of as-cast Ti-6Al-4V.

Potentiodynamic Polarization Test

Figure 3 shows the potentiodynamic polarization curve of the sample in Hank's solution at 37°C. Typically, the sample is passivated after the anodic activation zone as an indication of nearly constant passivation current density. Such a typical electrochemical behavior is frequently observed in valve metals (Qin et al., 2019). After fitting the potentiodynamic polarization curve, it shows that the corrosion potential of as-cast Ti-6Al-4V in Hank's solution at 37°C is -0.405 ± 0.027 V_{SCE}. The corrosion potential indicates the energy needed for corrosion reaction of a specific alloy in a specific corrosive environment (Chen et al., 2017a). The corrosion current density of as-cast Ti-6Al-4V is 0.031 ± 0.008 μA cm^{-2}. The corrosion current density illustrates the spontaneous corrosion rate of a specific alloy at the corrosion potential (Chen et al., 2017a). The data of both corrosion potential and corrosion current density fall in the outcomes in the literature, indicating the reliability of the potentiodynamic polarization test in this work. As seen from **Figure 3**, when the applied anodic potential exceeds a certain value, the passivation current density keeps almost constant as the applied anodic potential increases (Qin et al., 2017; Zhang et al., 2019a; Zhang et al., 2019b). The passivation current density is nearly constant from the potential of 0 V_{SCE} to 1.2 V_{SCE}. For Ti and Ti alloys, transpassive behavior is often observed (Narayanan and Seshadri, 2008; Qin et al., 2019; Seo and Lee, 2019). In this work, the transpassivation range is observed from 1.2 V_{SCE} to 1.5 V_{SCE}. The

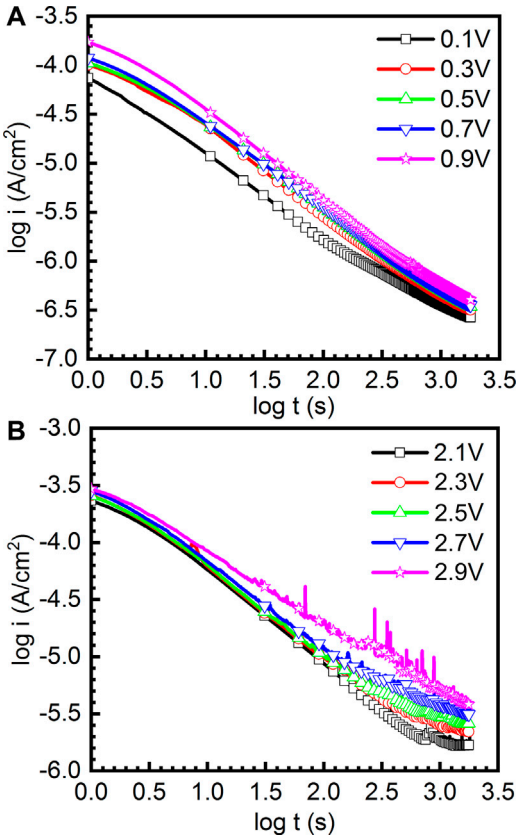

FIGURE 4 | Double-log plots of current-time of as-cast Ti-6Al-4V in the potentiostatic polarization tests under different file formation potentials in Hank's solution at 37°C, **(A)** the curves obtained under 0.1-0.9 V and **(B)** the curves obtained under 2.1-2.9 V.

current density rapidly increases with increasing the applied potential. When the applied potential reaches 1.5 V_{SCE}, the repassivation behavior of Ti-6Al-4V takes place. The passivation current density of Ti-6Al-4V slowly increases with increasing the applied potential in the repassivation range. Meanwhile, another feature can be observed. In the passivation range, the potentiodynamic polarization curve is significantly smooth. However, in the repassivation range, the potentiodynamic polarization curve is not smooth but has several stabs. Such stabs are indicative of metastable pitting corrosion (Frankel, 1998). Such a finding indicates the passivation of Ti-6Al-4V is imperfect in the repassivation range. According to the results of potentiodynamic polarization tests, the film formation potentials for potentiostatic polarization tests are selected at 0.1–0.9 V_{SCE} and 2.1~2.9 V_{SCE} in the following.

Potentiostatic Polarization Tests

It has been widely reported that the current density of the sample decreases quickly within the first 30 s and then slowly decreases to a nearly stable value due to the formation of the passive film (Gai et al., 2018). Therefore, the growth kinetics of passive film follows the Macdonald model (Lakatos-Varsányi et al., 1998), which can be expressed as the following equation:

$$\log i = \log A - n \log t, \quad (1)$$

where i is the current density, t is the passive time, and A and n are constants. The value of n can be used to indicate the growth rate of the passive film. **Figure 4** reveals the double-log plots of current-time of as-cast Ti-6Al-4V in the potentiostatic polarization tests in the passivation range and repassivation range in Hank's solution at 37°C, respectively. It can be found that the double-log plots of current-time are basically linear and the current density of the sample at high potential is always greater than that at low potential. Basically, n in **Eq. (1)** tending to be −1 illustrates that the growth process is primarily determined by the electrical field to generate a compact and protective passive film (Galvele et al., 1990). In **Figure 4A**, the values of n are −0.857, −0.912, −0.877, −0.859, and −0.935 for the double-log plots of current-time obtained at 0.1 V_{SCE}, 0.3 V_{SCE}, 0.5 V_{SCE}, 0.7 V_{SCE}, and 0.9 V_{SCE}. In **Figure 4B**, the values of n are −0.816, −0.834, −0.835, −0.788, and −0.713 for the double-log plots of current-time obtained at 2.1 V_{SCE}, 2.3 V_{SCE}, 2.5 V_{SCE}, 2.7 V_{SCE}, and 2.9 V_{SCE}. Based on these results, the passive films formed at the passivation range have higher quality than those formed at the repassivation range. Meanwhile, similar to the results presented in **Figure 3**, the curves obtained at the passivation range (0.1~0.9 V_{SCE}) are smooth. By contrast, the curves obtained at the passivation range are not smooth. Some features of metastable pitting corrosion are found. In particular, at the applied potential of 2.9 V_{SCE}, the metastable pitting corrosion is significantly obvious. The pitting corrosion results from the rupture of passive films form on the Ti and Ti alloys. If the rupture of passive films is healed by the passivation ability of alloys, the pitting corrosion is defined as the metastable pitting corrosion. If the rupture of passive films is not healed, the pitting corrosion is stable pitting corrosion. Generally, such stabs in the curves of current density (including **Figures 3**, **4**) indicate the rupture and healing of passive film (Dai et al., 2016a; Dai et al., 2016b; Qin et al., 2018). The higher applied anodic potential provides a higher capability to adsorb the anions, including halide ions (Basame and White, 2000). The halide ions are well known as one of the factors to trigger the metastable pitting corrosion, even stable pitting corrosion for the passive metals. Therefore, lots of metastable pitting corrosion phenomena are

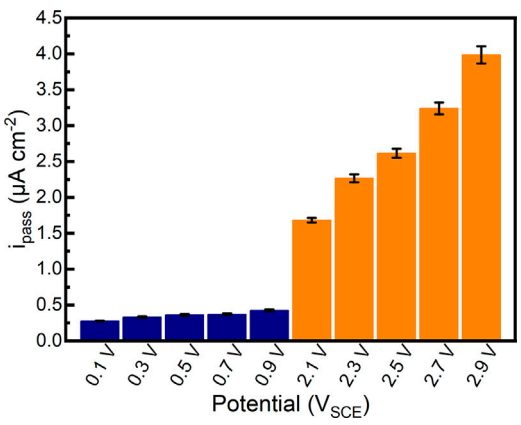

FIGURE 5 | Quasi-steady passivation current densities of as-cast Ti-6Al-4V in potentiostatic polarization tests under different applied potentials in Hank's solution at 37°C.

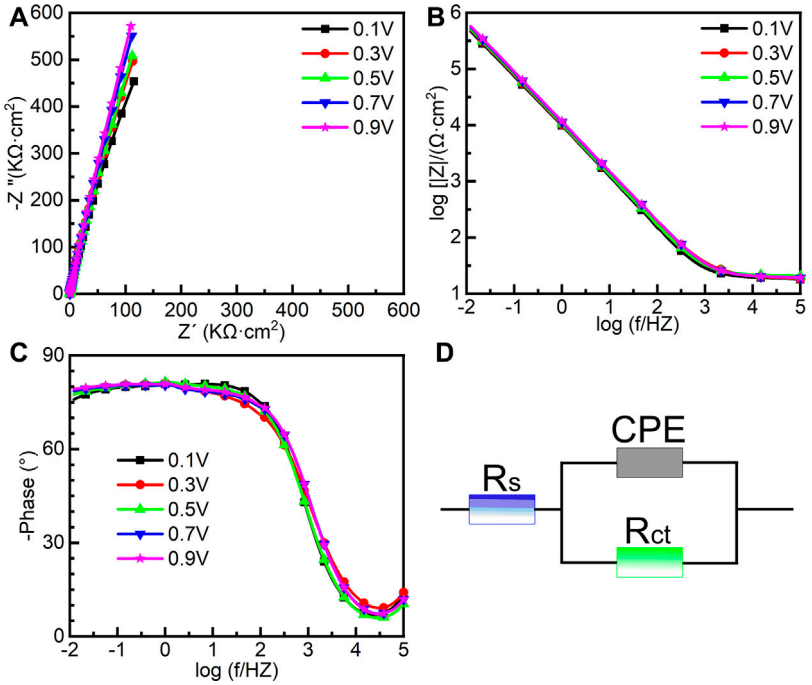

FIGURE 6 | Electrochemical impedance spectroscopy of as-cast Ti-6Al-4V under different film formation potentials in passivation range in Hank's solution at 37°C, **(A)** Nyquist plots, **(B)** Bode impedance plots, **(C)** Bode phase diagram and **(D)** equivalent circuit.

observed under high potential. Such a phenomenon is always associated with the sudden increase and subsequent decrease in the current density. This finding reflects the low quality of passive film formed on the sample at the applied potential of 2.9 V_{SCE}.

After 1800 s potentiostatic polarization tests in Hank's solution at 37°C, the passivation current densities of the samples almost reach stability. The quasi-steady passivation current densities of samples are shown in **Figure 5**. It can be found that the quasi-steady passivation current densities of samples gradually increase from 0.276 μA cm^{-2} to 0.425 μA cm^{-2} in the passivation range. In comparison, the quasi-steady passivation current densities of samples significantly increase to 1.682 μA cm^{-2}–3.985 μA cm^{-2} in the repassivation range, which is increased by an order of magnitude. The quasi-steady passivation current densities could elucidate the migration of ions at a specific potential (Chen et al., 2017b; Guan et al., 2018). Although the alloy can be regarded as the stable passivation state in the current situation, the quasi-steady passivation current density illustrates the balance of the formation and dissolution of the passive film. According to Faraday's law, higher quasi-steady passivation current density is related to the smaller impedance of passive film (Vautrin-Ul et al., 2007). Therefore, such a finding may specify that the quality of passive films formed on as-cast Ti-6Al-4V in the repassivation range is not as good as that formed on as-cast Ti-6Al-4V in the passivation range.

Electrochemical Impedance Spectroscopy

To further investigate the electrochemical system at the metal/solution interfaces, EIS was conducted on the samples polarized under different potentials in Hank's solution at 37°C. **Figure 6** shows the EIS results of the samples on which the potentiostatic polarization tests were conducted at 0.1~0.9 V_{SCE}, including the Nyquist diagram, Bode plot, and equivalent circuit diagram. **Figure 6A** is the Nyquist plots. All Nyquist plots have only one capacitor arc, which has a very large radius. The radius of the capacitor arc increases with increasing the film formation potential. From the Bode plots (**Figures 6B, C**), it is hard to distinguish the difference among the five samples. By fitting the EIS data using the equivalent circuit diagram in **Figure 6D**, the impedance information of passive films formed on the samples at different potentials can be obtained. In this equivalent circuit diagram (**Figure 6D**), R_s and R_{ct} correspond to the solution resistance and charge transfer resistance, respectively. Because of the influence of the surface roughness, the constant phase element (CPE) is used (Chen et al., 2018d; Liang et al., 2018; Yang et al., 2018). n is the parameter of CPE. For $n = 1$, CPE is regarded as an ideal capacitor, whereas CPE is nonideal when $0.5 < n < 1$ (Zhang et al., 2020a). The fitted results of EIS are listed in **Table 1**.χ^2 is the sum of the square of the difference between theoretical and experimental points, which is lower than 0.007, indicating a good quality of the fitting in this experiment. These results show that the values of R_s for all tests are almost the same. However, there is a significant distinction in the values of R_{ct}. For the sample on which the potentiostatic polarization test was conducted at 0.1 V_{SCE}, the value of R_{ct} is 1.86 ± 0.10 MΩ cm^2. The values of R_{ct} increase with the increasing film formation potential. When the film formation potential is 0.9 V_{SCE}, the value of R_{ct} reaches 4.35 ± 1.21 MΩ cm^2. R_{ct} indicates the impedance of electrons from the metal to the solution. Therefore, the higher value of R_{ct} illustrates the higher protectiveness of passive film. Such a result is consistent with the outcome in the other works (Shibata and Zhu, 1994).

TABLE 1 | Fitting results of electrochemical impedance spectra for as-cast Ti–6Al–4V after OCP tests in Hank's solutions at 37°C. R_s means solution resistance, R_{ct} indicates charge transfer resistance, CPE describes charge transfer capacitance, *n* is the exponent of CPE, and χ^2 is the sum of the square of the difference between theoretical and experimental points.

Potential (V_{SCE})	R_s ($\Omega \cdot cm^2$)	*n*	R_{ct} ($M\Omega \cdot cm^2$)	CPE × 10^{-5} ($F \cdot cm^{-2}$)	χ^2
0.1	18.01 ± 0.89	0.8654 ± 0.072	1.86 ± 0.10	2.24 ± 0.12	3.03×10^{-3}
0.3	17.64 ± 0.72	0.8601 ± 0.090	2.76 ± 0.30	1.87 ± 0.57	1.14×10^{-3}
0.5	16.70 ± 0.86	0.9049 ± 0.008	3.34 ± 0.03	1.92 ± 0.02	6.37×10^{-3}
0.7	19.18 ± 0.80	0.9081 ± 0.003	3.26 ± 1.10	2.12 ± 0.43	1.53×10^{-3}
0.9	18.94 ± 1.20	0.8997 ± 0.005	4.35 ± 1.21	2.01 ± 0.05	2.75×10^{-3}

EIS was also conducted in the repassivation range in order to understand the electrochemical system at the metal/solution interfaces after transpassivation. **Figure 7** shows the Nyquist diagram, Bode plot, and the equivalent circuit diagram used for the samples on which the potentiostatic polarization tests were conducted at 2.1~2.9 V_{SCE}. The impedance of passive film formed in the range of 2.1~2.9 V_{SCE} (**Figure 7A**) is significantly larger than that in the range of 0.1~0.9 V_{SCE} (**Figure 6A**). Such a result is in line with the outcomes in the literature that the thickness of the passive film formed on Ti and Ti alloys increases with increasing the applied anodic potential (Al-Mayouf et al., 2004; Guan et al., 2018). The Bode phase angle plot in **Figure 7C** is also different from that in **Figure 6C**. In **Figure 6C**, the curve from 10^2 Hz to 10^{-2} Hz is a wide plateau. In comparison, the curve from 10^2 Hz to 10^{-2} Hz has dual dumps in **Figure 7C**. Such a finding illustrates that the passive film formed on the samples in the repassivation range may have a bilayer structure, namely, the inner barrier layer and outer porous layer (Aziz-Kerrzo et al., 2001). **Table 2** lists the fitting results of EIS in **Figure 7**. Different equivalent circuits are used for fitting EIS of different-structured passive films. Therefore, for this EIS, a R(Q(R(QR)) equivalent circuit diagram is used to highlight the outer porous layer on the polarized sample. R_s, R_{ct}, and CPE have the same meaning as **Figure 6**. R_f is the film resistance, which illustrates the diffusion resistance in the defects of the outer porous layer (Zhang et al., 2020a). χ^2 is lower than 0.0007, which also indicates a good quality of the fitting. Apparently, R_f is significantly lower than R_{ct}. Therefore, the corrosion resistance (as well as the impedance of passive film) of the polarized sample strongly depends on the value of R_{ct}. The value of R_{ct} for the sample polarized at 2.1 V_{SCE} is 7.691 ± 1.203 $M\Omega\ cm^2$, which is nearly two times that for the sample polarized at 0.9 V_{SCE}. Such a finding demonstrates that the impedance of passive film formed on the as-cast Ti-6Al-4V increases with increasing the applied potential regardless of the occurrence of transpassive behavior. With the continuous

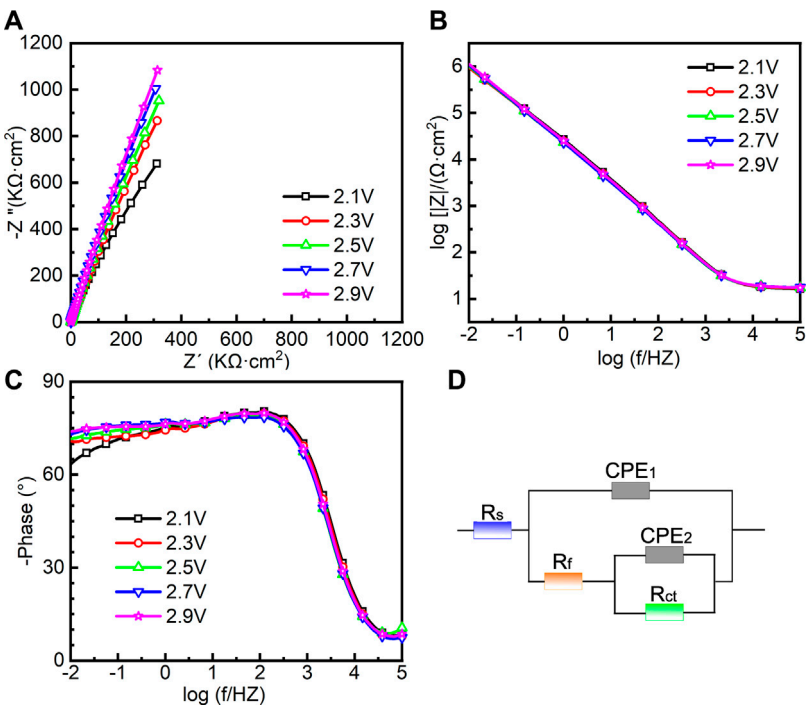

FIGURE 7 | Electrochemical impedance spectroscopy of as-cast Ti-6Al-4V under different film formation potentials in the repassivation range in Hank's solution at 37°C, **(A)** Nyquist plots, **(B)** Bode impedance plots, **(C)** Bode phase diagram and **(D)** equivalent circuit.

TABLE 2 | Fitting results of electrochemical impedance spectra for as-cast Ti–6Al–4V after OCP tests in Hank's solutions at 37°C. R_s means solution resistance, R_f is film resistance, R_{ct} indicates charge transfer resistance, CPE_1 and CPE_2 describe film capacitance and charge transfer capacitance, n_1 and n_2 are the exponents of CPE_1 and CPE_2, and χ^2 is the sum of the square of the difference between theoretical and experimental points.

Potential (V_{SCE})	R_s ($\Omega \cdot cm^2$)	R_f ($k\Omega \cdot cm^2$)	n_1	$CPE_1 \times 10^{-6}$ ($F \cdot cm^{-2}$)	R_{ct} ($M\Omega \cdot cm^2$)	$CPE_2 \times 10^{-5}$ ($F \cdot cm^{-2}$)	n_2	χ^2
2.1	15.05 ± 1.28	6.191 ± 0.50	0.8018 ± 0.050	7.19 ± 0.84	7.691 ± 1.20	2.109 ± 0.08	0.9266 ± 0.052	5.71×10^{-4}
2.3	16.03 ± 1.12	6.728 ± 0.02	0.8306 ± 0.061	7.15 ± 0.52	14.587 ± 1.11	2.425 ± 0.65	0.8316 ± 0.104	3.47×10^{-4}
2.5	13.26 ± 2.55	7.495 ± 0.52	0.7919 ± 0.098	5.66 ± 0.32	18.337 ± 1.72	2.972 ± 0.04	0.9409 ± 0.060	4.08×10^{-4}
2.7	15.66 ± 1.83	7.570 ± 0.20	0.8608 ± 0.088	6.30 ± 0.69	24.580 ± 2.86	3.449 ± 0.86	0.9084 ± 0.037	6.11×10^{-4}
2.9	14.19 ± 0.20	8.027 ± 0.06	0.7717 ± 0.006	7.33 ± 0.05	27.143 ± 2.74	2.226 ± 0.08	0.9805 ± 0.012	3.73×10^{-4}

increase in the applied potential, the value of R_{ct} reaches 27.143 ± 2.74 MΩ cm^2 for the sample polarized at 2.9 V_{SCE}. Therefore, the passive film formed on the sample polarized at 2.9 V_{SCE} has the best protectiveness in all samples used in this work.

Growth of Passive Films

According to the anodic oxidation theory, the thickness of the passive film is almost linearly dependent on the applied potential (Liu et al., 2004). Therefore, the thicknesses of passive films (L_{SS}) formed on samples polarized at different passivation ranges were calculated by the following equation:

$$L_{SS} = \frac{\varepsilon \varepsilon_0 A}{C_{\text{eff}}}, \tag{2}$$

where ε is the relative dielectric constant (60 for TiO_2 (Gai et al., 2018)), ε_0 is the vacuum dielectric constant (8.85×10^{-14} F cm^{-1}), A is the area of Ti electrode, and C_{eff} is the effective capacitance. By processing the EIS data using ZsimpWin software, the capacitance vs. frequency curves of the polarized samples could be obtained. The capacitance at 1 kHz was selected as effective capacitance (Guan et al., 2018). Based on the calculation using **Eq. 1**, the thicknesses of passive films formed on samples polarized at different passivation ranges are shown in **Figure 8**. **Figure 8A** shows the thicknesses of passive films formed on samples polarized in the passivation range. The thicknesses of passive films basically obey the linear relationship with the film formation potential, which is consistent with the anodic oxidation theory. As seen from the fitting result, the slope of the fitted line is 3.30 nm/V_{SCE}. This result means that the passive film has an increase of 3.30 nm per V_{SCE}. The thicknesses of passive films also obey the linear relationship with the film formation potential in the repassivation range. However, the slope of the fitted line in **Figure 8B** is different from that in **Figure 8A**. The passive film grows at a growth rate of 3.84 nm/V_{SCE} in the repassivation range, which is higher than that in the passivation range. Therefore, one can conclude that the as-cast Ti-6Al-4V has distinct passive film growth rates in different passivation range.

Possible Film Formation Mechanism Before and After Transpassivation

As is well known, the quality of formed passive films determines the corrosion resistance of passive metals in corrosive environments (Chen et al., 2015a; Chen et al., 2016). The criterion for the quality of passive films may be varied in line with different purposes (Lu et al., 2008; Zhang et al., 2019b). In this work, an apparent transpassivation range is found before the passivation range and repassivation range. Both passivation current densities and quasi-steady passivation current densities of the samples in the potentiodynamic polarization and potentiostatic polarization significantly increase in the repassivation range as compared to those in the passivation range (**Figures 3**, **5**). The passivation current densities illustrate the ionic migration in the passive films formed on the samples at the given potentials, namely, the exchange of substances between the sample and corrosive environment (Huang and Blackwood, 2005). Therefore, it can be confirmed that the higher film formation potential results in a higher film growth rate and a higher film dissolution rate (**Figure 5**). Although the passive films formed under higher applied potentials show a higher impedance, the higher passivation current densities of the samples also indicate the higher corrosion rates under the given applied potentials. Therefore, two questions can be divided hereafter. The as-cast Ti-6Al-4V may have a higher corrosion rate at a higher applied potential, hence it can not be applied as an electrode (or other equivalents) under a high potential. However, the passive film formed under the high potential has high impedance. Therefore, the polarized as-cast Ti-6Al-4V can be used as the workpiece (or part) in a corrosive environment without applied potential (such as the human body). Such a polarized as-cast Ti-6Al-4V would possess superior corrosion resistance due to the high-impedance passive film.

The applied potential provides the higher driving force to adsorb the negative ions in the electrolyte and also increases the electric field in the passive film (DespiĆ et al., 1988). Within the adsorbed negative ions, OH^- or O^{2-} forms TiO_2 (Zhang et al., 2020b). As such, the thickness of passive film always increases with increasing applied potential. However, the higher applied potential also would adsorb more ingress ions (such as halide ions). Such ingress ions would trigger the localized breakdown of passive film (Zhang et al., 2018), which is observed in the samples polarized at 2.9 V_{SCE} (**Figure 5**). According to the point defect model, the pitting corrosion or metastable pitting corrosion results from the condensation of cation vacancies catalyzed by aggressive ions (Macdonald, 2011). Based on the existing data, the density of oxygen vacancies in the passive films formed on Ti-6Al-4V decreases with increasing applied potential (Jia et al., 2016; Gai et al., 2018). Hence, to achieve the condensation of oxygen vacancies, a high electric field in the passive film is required. As discussed above, the sample polarized under higher applied potential shows higher steady-state passivation current density. Such a phenomenon also demonstrates a higher electric field in the passive film. The higher electric field directly results in the high

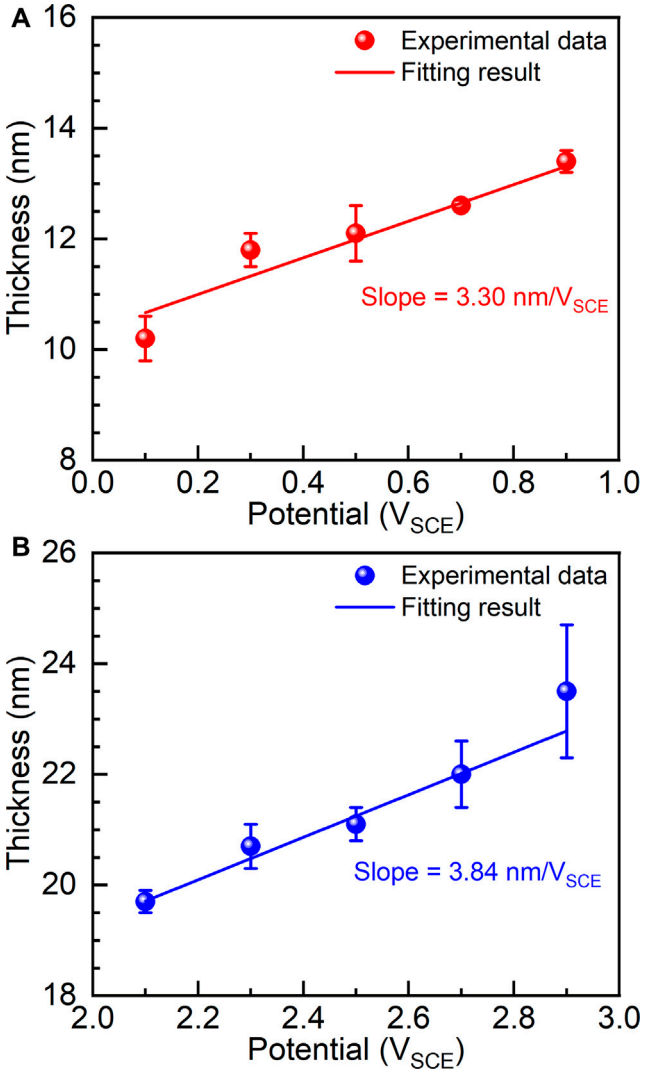

FIGURE 8 | Thicknesses of passive films formed on as-cast Ti-6Al-4V under different film formation potentials, **(A)** films formed between 0.1 V and 0.9 V and **(B)** films formed between 2.1 V and 2.9 V.

diffusion coefficient of oxygen vacancies (Lu et al., 2009; Guan et al., 2018). The flux of oxygen vacancies is the function of the density of oxygen vacancies and their diffusion coefficient. A high flux of oxygen vacancies could result in the condensation of cation vacancies. Due to observed high possibility of metastable pitting corrosion under high applied potential (repassivation range), one can conclude that the applied potential is decisive for the localized destruction of the passive film.

CONCLUSION

In this work, the electrochemical behavior of as-cast Ti-6Al-4V in Hank's solution at 37 °C before and after transpassivation was investigated. After carefully analyzing the microstructure of as-cast Ti-6Al-4V, the potentiodynamic polarization test was conducted to confirm the passivation and repassivation ranges. By investigating the electrochemical impedance spectroscopy of the samples polarized in passivation and repassivation ranges, characteristics of passive films formed on as-cast Ti-6Al-4V are further understood. Some key conclusions are drawn as follows.

(1) In the potentiodynamic polarization test, the passivation range is observed from 0 V_{SCE} to 1.2 V_{SCE} for the sample. Subsequently, the transpassivation behavior of the sample is found from 1.2 V_{SCE} to 1.5 V_{SCE}. Afterward, the repassivation range is observed from 1.5 V_{SCE} to the end of the test.
(2) Potentiostatic polarization tests were conducted at 0.1~0.9 V_{SCE} and 2.1~2.9 V_{SCE} to produce passive films on the samples. The growth kinetics of the passive film follows the Macdonald model. With increasing the film formation potential, the quasi-steady passivation current densities of as-cast Ti-6Al-4V increase. Metastable pitting corrosion is observed under the applied potentials of 2.7 V_{SCE} and 2.9 V_{SCE}.
(3) Electrochemical impedance spectroscopy examinations were carried out on the potentiostatic polarized samples. The results show that the thickness of the passive film as well as the charge transfer of the samples increases with increasing the applied potential. The formed passive films before and after transpassivation have different growth rates, which are calculated as 3.30 nm/V_{SCE} and 3.84 nm/V_{SCE} in the passivation range and repassivation range.
(4) Based on the result of this work, one can conclude that the passive film formed under high applied potential has better protectiveness. Therefore, although the transpassivation behavior may destroy the passive film to some extent, the passive film formed under higher applied potential still has higher impedance. However, the higher applied potential also provides the higher driving force to adsorb the aggressive ions in the electrolyte and also increases the electric field in the passive film. Therefore, metastable pitting corrosion is observed at the high applied potential.

DATA AVAILABILITY STATEMENT

The original contributions presented in the study are included in the article/Supplementary Material, further inquiries can be directed to the corresponding author.

AUTHOR CONTRIBUTIONS

GY and XL conceived and designed the experiments; HZ performed experiments; CH and Y-WC analyzed the data; GY, CZ, and SL wrote the paper.

FUNDING

The study was funded by Postgraduate Research & Practice Innovation Program of Jiangsu Province.

REFERENCES

Al-Mayouf, A. M., Al-Swayih, A. A., and Al-Mobarak, N. A. (2004). Effect of potential on the corrosion behavior of a new titanium alloy for dental implant applications in fluoride media. *Mater. Corros.* 55 (2), 88–94. doi:10.1002/maco.200303697

Aladjem, A. (1973). Anodic oxidation of titanium and its alloys. *J. Mater. Sci.* 8 (5), 688–704. doi:10.1007/bf00561225

Aziz-Kerrzo, M., Conroy, K. G., Fenelon, A. M., Farrell, S. T., and Breslin, C. B. (2001). Electrochemical studies on the stability and corrosion resistance of titanium-based implant materials. *Biomaterials* 22 (12), 1531–1539. doi:10.1016/s0142-9612(00)00309-4

Babilas, D., Urbańczyk, E., Sowa, M., Maciej, A., Korotin, D. M., Zhidkov, I. S., et al. (2016). On the electropolishing and anodic oxidation of Ti-15Mo alloy. *Electrochim. Acta.* 205, 256–265. doi:10.1016/j.electacta.2016.01.218

Bai, Y., Gai, X., Li, S., Zhang, L.-C., Liu, Y., Hao, Y., et al. (2017). Improved corrosion behaviour of electron beam melted Ti-6Al–4V alloy in phosphate buffered saline. *Corrosion Sci.* 123, 289–296. doi:10.1016/j.corsci.2017.05.003

Balla, V. K., Banerjee, S., Bose, S., and Bandyopadhyay, A. (2010). Direct laser processing of a tantalum coating on titanium for bone replacement structures. *Acta Biomater.* 6 (6), 2329–2334. doi:10.1016/j.actbio.2009.11.021

Basame, S. B., and White, H. S. (2000). Pitting corrosion of titanium the relationship between pitting potential and competitive anion adsorption at the oxide film/electrolyte interface. *J. Electrochem. Soc.* 147 (4), 1376. doi:10.1149/1.1393364

Chai, L., Chen, K., Zhi, Y., Murty, K. L., Chen, L. Y., and Yang, Z. (2018). Nanotwins induced by pulsed laser and their hardening effect in a Zr alloy. *J. Alloys Compd.* 748, 163–170. doi:10.1016/j.jallcom.2018.03.126

Chai, L. J., Wang, S. Y., Wu, H., Guo, N., Pan, H. C., Chen, L. Y., et al. (2017). $\alpha \rightarrow \beta$ transformation characteristics revealed by pulsed laser-induced non-equilibrium microstructures in duplex-phase Zr alloy. *Sci. China Technol. Sci.* 60 (8), 1255–1262. doi:10.1007/s11431-016-9038-y

Chen, L.-Y., Cui, Y.-W., and Zhang, L.-C. (2020a). Recent development in beta titanium alloys for biomedical applications. *Metals* 10 (9), 1139. doi:10.3390/met10091139

Chen, L.-Y., Wang, H., Zhao, C., Lu, S., Wang, Z.-X., Sha, J., et al. (2019a). Automatic remelting and enhanced mechanical performance of a plasma sprayed NiCrBSi coating. *Surf. Coating. Technol.* 369, 31–43. doi:10.1016/j.surfcoat.2019.04.052

Chen, L.-Y., Xu, T., Lu, S., Wang, Z.-X., Chen, S., and Zhang, L.-C. (2018a). Improved hardness and wear resistance of plasma sprayed nanostructured NiCrBSi coating via short-time heat treatment. *Surf. Coating. Technol.* 350, 436–444. doi:10.1016/j.surfcoat.2018.07.037

Chen, L.-Y., Xu, T., Wang, H., Sang, P., Lu, S., Wang, Z.-X., et al. (2019b). Phase interaction induced texture in a plasma sprayed-remelted NiCrBSi coating during solidification: an electron backscatter diffraction study. *Surf. Coating. Technol.* 358, 467–480. doi:10.1016/j.surfcoat.2018.11.019

Chen, L., Huang, J., Lin, C., Pan, C., Chen, S., Yang, T., et al. (2017a). Anisotropic response of Ti-6Al-4V alloy fabricated by 3D printing selective laser melting. *Mater. Sci. Eng. A* 682, 389–395. doi:10.1016/j.msea.2016.11.061

Chen, L., Li, J., Zhang, Y., Zhang, L. C., Lu, W., Wang, L., et al. (2015a). Zr-Sn-Nb-Fe-Si-O alloy for fuel cladding candidate: processing, microstructure, corrosion resistance and tensile behavior. *Corrosion Sci.* 100, 332–340. doi:10.1016/j.corsci.2015.08.005

Chen, L., Li, J., Zhang, Y., Zhang, L. C., Lu, W., Zhang, L., et al. (2015b). Effects of alloyed Si on the autoclave corrosion performance and periodic corrosion kinetics in Zr-Sn-Nb-Fe-O alloys. *Corrosion Sci.* 100, 651–662. doi:10.1016/j.corsci.2015.08.043

Chen, L. Y., Sang, P., Zhang, L., Song, D., Chu, Y. Q., Chai, L., et al. (2018b). Homogenization and growth behavior of second-phase particles in a deformed Zr-Sn-Nb-Fe-Cu-Si-O alloy. *Metals* 8 (10), 759. doi:10.3390/met8100759

Chen, L. Y., Shen, P., Zhang, L., Lu, S., Chai, L., Yang, Z., et al. (2018c). Corrosion behavior of non-equilibrium Zr-Sn-Nb-Fe-Cu-O alloys in high-temperature 0.01 M LiOH aqueous solution and degradation of the surface oxide films. *Corrosion Sci.* 136, 221–230. doi:10.1016/j.corsci.2018.03.012

Chen, L., Zeng, Q., Li, J., Lu, J., Zhang, Y., Zhang, L.-C., et al. (2016). Effect of microstructure on corrosion behavior of a Zr-Sn-Nb-Fe-Cu-O alloy. *Mater. Des.* 92, 888–896. doi:10.1016/j.matdes.2015.12.067

Chen, Q., and Thouas, G. A. (2015). Metallic implant biomaterials. *Mater. Sci. Eng. R Rep.* 87, 1–57. doi:10.1016/j.mser.2014.10.001

Chen, W., Xu, J., Liu, D., Bao, J., Sabbaghianrad, S., Shan, D., et al. (2020b). Microstructural evolution and microhardness variations in pure titanium processed by high-pressure torsion. *Adv. Eng. Mater.* 22 (6), 1901462. doi:10.1002/adem.201901462

Chen, Y., Zhang, J., Dai, N., Qin, P., Attar, H., and Zhang, L.-C. (2017b). Corrosion behaviour of selective laser melted Ti-TiB biocomposite in simulated body fluid. *Electrochim. Acta.* 232, 89–97. doi:10.1016/j.electacta.2017.02.112

Chen, Y., Zhang, J., Gu, X., Dai, N., Qin, P., and Zhang, L. C. (2018d). Distinction of corrosion resistance of selective laser melted Al-12Si alloy on different planes. *J. Alloys Compd.* 747, 648–658. doi:10.1016/j.jallcom.2018.03.062

Dai, N., Zhang, J., Chen, Y., and Zhang, L.-C. (2017). Heat treatment degrading the corrosion resistance of selective laser melted Ti-6Al-4V alloy. *J. Electrochem. Soc.* 164 (7), C428–C434. doi:10.1149/2.1481707jes

Dai, N., Zhang, L.-C., Zhang, J., Chen, Q., and Wu, M. (2016a). Corrosion behavior of selective laser melted Ti-6Al-4V alloy in NaCl solution. *Corrosion Sci.* 102, 484–489. doi:10.1016/j.corsci.2015.10.041

Dai, N., Zhang, L.-C., Zhang, J., Zhang, X., Ni, Q., Chen, Y., et al. (2016b). Distinction in corrosion resistance of selective laser melted Ti-6Al-4V alloy on different planes. *Corrosion Sci.* 111, 703–710. doi:10.1016/j.corsci.2016.06.009

Dehghanghadikolaei, A., Ibrahim, H., Amerinatanzi, A., Hashemi, M., Moghaddam, N. S., and Elahinia, M. (2019). Improving corrosion resistance of additively manufactured nickel–titanium biomedical devices by micro-arc oxidation process. *J. Mater. Sci.* 54 (9), 7333–7355. doi:10.1007/s10853-019-03375-1

Despić, A. R., DražIć, D. M., and Gajić-Krstajić, U. (1988). Effect of the addition of chloride on the anodic dissolution of aluminium through barrier films. *J. Electroanal. Chem. Interfacial Electrochem.* 242 (1-2), 303–315. doi:10.1016/0022-0728(88)80259-6

Frankel, G. S. (1998). Pitting corrosion of metals a review of the critical factors. *J. Electrochem. Soc.* 145, 2186–2198.

Gai, X., Bai, Y., Li, J., Li, S., Hou, W., Hao, Y., et al. (2018). Electrochemical behaviour of passive film formed on the surface of Ti-6Al-4V alloys fabricated by electron beam melting. *Corrosion Sci.* 145, 80–89. doi:10.1016/j.corsci.2018.09.010

Galvele, J., Torresi, R., and Carranza, R. (1990). Passivity breakdown, its relation to pitting and stress-corrosion-cracking processes. *Corrosion Sci.* 31, 563–571. doi:10.1016/0010-938x(90)90163-y

Guan, L., Li, Y., Wang, G., Zhang, Y., and Zhang, L.-C. (2018). pH dependent passivation behavior of niobium in acid fluoride-containing solutions. *Electrochim. Acta.* 285, 172–184. doi:10.1016/j.electacta.2018.07.221

Hanawa, T. (2004). Metal ion release from metal implants. *Mater. Sci. Eng. C* 24 (6–8), 745–752. doi:10.1016/j.msec.2004.08.018

Huang, Y. Z., and Blackwood, D. J. (2005). Characterisation of titanium oxide film grown in 0.9% NaCl at different sweep rates. *Electrochim. Acta.* 51 (6), 1099–1107. doi:10.1016/j.electacta.2005.05.051

Jaeggi, C., Frauchiger, V., Eitel, F., Stiefel, M., Schmotzer, H., and Siegmann, S. (2011). The effect of surface alloying of Ti powder for vacuum plasma spraying of open porous titanium coatings. *Acta Mater.* 59 (2), 717–725. doi:10.1016/j.actamat.2010.10.010

Jia, Z., Duan, X., Zhang, W., Wang, W., Sun, H., Wang, S., et al. (2016). Ultra-sustainable $Fe_{78}Si_9B_{13}$ metallic glass as a catalyst for activation of persulfate on methylene blue degradation under UV-Vis light. *Sci. Rep.* 6 (1), 38520. doi:10.1038/srep38520

Kang, L., and Yang, C. (2019). A review on high-strength titanium alloys: microstructure, strengthening, and properties. *Adv. Eng. Mater.* 21 (8), 1801359. doi:10.1002/adem.201801359

Kong, D.-S., and Wu, J.-X. (2007). An electrochemical study on the anodic oxygen evolution on oxide film covered titanium. *J. Electrochem. Soc.* 155 (1), C32. doi:10.1149/1.2799731

Lakatos-Varsányi, M., Falkenberg, F., and Olefjord, I. (1998). The influence of phosphate on repassivation of 304 stainless steel in neutral chloride solution. *Electrochim. Acta.* 43 (1-2), 187–197. doi:10.1016/s0013-4686(97)00224-7

Lei, X., Dong, L., Zhang, Z., Liu, Y., Hao, Y., Yang, R., et al. (2017). Microstructure, texture evolution and mechanical properties of VT3-1 titanium alloy processed by multi-pass drawing and subsequent isothermal annealing. *Metals* 7 (4), 131. doi:10.3390/met7040131

Liang, S. X., Jia, Z., Liu, Y. J., Zhang, W., Wang, W., Lu, J., et al. (2018). Compelling rejuvenated catalytic performance in metallic glasses. *Adv. Mater.* 30 (45), e1802764. doi:10.1002/adma.201802764

Liu, S., Han, S., Zhang, L., Chen, L.-Y., Wang, L., Zhang, L., et al. (2020a). Strengthening mechanism and micropillar analysis of high-strength NiTi–Nb eutectic-type alloy prepared by laser powder bed fusion. *Compos. B. Eng.* 200, 108358. doi:10.1016/j.compositesb.2020.108358

Liu, S., Liu, J., Wang, L., Ma, R. L. W., Zhong, Y., Lu, W., et al. (2020b). Superelastic behavior of in-situ eutectic-reaction manufactured high strength 3D porous NiTi-Nb scaffold. *Scripta Mater.* 181, 121–126. doi:10.1016/j.scriptamat.2020.02.025

Liu, X., Chu, P. K., and Ding, C. (2004). Surface modification of titanium, titanium alloys, and related materials for biomedical applications. *Mater. Sci. Eng. R* 47 (3-4), 49–121. doi:10.1016/j.mser.2004.11.001

Lu, H.-B., Poh, C.-K., Zhang, L. C., Guo, Z. P., Yu, X. B., and Liu, H.-K. (2009). Dehydrogenation characteristics of Ti-and Ni/Ti-catalyzed Mg hydrides. *J. Alloys Compd.* 481 (1-2), 152–155. doi:10.1016/j.jallcom.2009.02.125

Lu, H., Zhang, L., Gebert, A., and Schultz, L. (2008). Pitting corrosion of Cu–Zr metallic glasses in hydrochloric acid solutions. *J. Alloys Compd.* 462 (1-2), 60–67. doi:10.1016/j.jallcom.2007.08.023

Macdonald, D. D. (2011). The history of the point defect model for the passive state: a brief review of film growth aspects. *Electrochim. Acta.* 56 (4), 1761–1772. doi:10.1016/j.electacta.2010.11.005

Montiel, A., Onofre, E., and Escudero, M. L. (2020). Synthesis and electrochemical characterisation of magnetite coatings on Ti6Al4V-ELI. *Metals* 10 (12), 1640. doi:10.3390/met10121640

Narayanan, R., and Seshadri, S. K. (2008). Point defect model and corrosion of anodic oxide coatings on Ti–6Al–4V. *Corrosion Sci.* 50 (6), 1521–1529. doi:10.1016/j.corsci.2008.02.023

Qin, P., Chen, Y., Liu, Y.-J., Zhang, J., Chen, L.-Y., Li, Y., et al. (2019). Resemblance in corrosion behavior of selective laser melted and traditional monolithic β Ti-24Nb-4Zr-8Sn alloy. *ACS Biomater. Sci. Eng.* 5 (2), 1141–1149. doi:10.1021/acsbiomaterials.8b01341

Qin, P., Liu, Y., Sercombe, T. B., Li, Y., Zhang, C., Cao, C., et al. (2018). Improved corrosion resistance on selective laser melting produced Ti-5Cu alloy after heat treatment. *ACS Biomater. Sci. Eng.* 4 (7), 2633–2642. doi:10.1021/acsbiomaterials.8b00319

Qin, X., Guo, X., Lu, J., Chen, L., Qin, J., and Lu, W. (2017). Erosion-wear and intergranular corrosion resistance properties of AISI 304L austenitic stainless steel after low-temperature plasma nitriding. *J. Alloys Compd.* 698, 1094–1101. doi:10.1016/j.jallcom.2016.12.164

Rabadia, C. D., Liu, Y. J., Chen, L. Y., Jawed, S. F., Wang, L. Q., Sun, H., et al. (2019a). Deformation and strength characteristics of Laves phases in titanium alloys. *Mater. Des.* 179, 107891. doi:10.1016/j.matdes.2019.107891

Rabadia, C. D., Liu, Y. J., Zhao, C. H., Wang, J. C., Jawed, S. F., Wang, L. Q., et al. (2019b). Improved trade-off between strength and plasticity in titanium based metastable beta type Ti-Zr-Fe-Sn alloys. *Mater. Sci. Eng. A* 766, 138340. doi:10.1016/j.msea.2019.138340

Rautray, T. R., Narayanan, R., and Kim, K. H. (2011). Ion implantation of titanium based biomaterials. *Prog. Mater. Sci.* 56 (8), 1137–1177. doi:10.1016/j.pmatsci.2011.03.002

Sabban, R., Bahl, S., Chatterjee, K., and Suwas, S. (2019). Globularization using heat treatment in additively manufactured Ti-6Al-4V for high strength and toughness. *Acta Mater.* 162, 239–254. doi:10.1016/j.actamat.2018.09.064

Sang, P., Chen, L.-Y., Zhao, C., Wang, Z.-X., Wang, H., Lu, S., et al. (2019). Particle size-dependent microstructure, hardness and electrochemical corrosion behavior of atmospheric plasma sprayed NiCrBSi coatings. *Metals* 9 (12), 1342. doi:10.3390/met9121342

Semenova, I. P., Polyakova, V. V., Dyakonov, G. S., and Polyakov, A. V. (2020). Ultrafine-Grained titanium-based alloys: structure and service properties for engineering applications. *Adv. Eng. Mater.* 22 (1), 1900651. doi:10.1002/adem.201900651

Seo, D.-I., and Lee, J.-B. (2019). Corrosion characteristics of additive-manufactured Ti-6Al-4V using microdroplet cell and critical pitting temperature techniques. *J. Electrochem. Soc.* 166 (13), C428–C433. doi:10.1149/2.0571913jes

Shibata, T., and Zhu, Y.-C. (1994). The effect of film formation potential on the stochastic processes of pit generation on anodized titanium. *Corrosion Sci.* 36 (1), 153–163. doi:10.1016/0010-938x(94)90116-3

Stolyarov, V. V., Shuster, L. S., Migranov, M. S., Valiev, R. Z., and Zhu, Y. T. (2004). Reduction of friction coefficient of ultrafine-grained CP titanium. *Mater. Sci. Eng. A* 371 (1-2), 313–317. doi:10.1016/j.msea.2003.12.026

Vautrin-Ul, C., Taleb, A., Stafiej, J., Chaussé, A., and Badiali, J. P. (2007). Mesoscopic modelling of corrosion phenomena: coupling between electrochemical and mechanical processes, analysis of the deviation from the Faraday law. *Electrochim. Acta.* 52 (17), 5368–5376. doi:10.1016/j.electacta.2007.02.051

Wang, L., Wang, C., Zhang, L. C., Chen, L., Lu, W., and Zhang, D. (2016). Phase transformation and deformation behavior of NiTi-Nb eutectic joined NiTi wires. *Sci. Rep.* 6 (1), 23905. doi:10.1038/srep23905

Wang, L., Qu, J., Chen, L., Meng, Q., Zhang, L. C., Qin, J., et al. (2015). Investigation of deformation mechanisms in β-type Ti-35Nb-2Ta-3Zr alloy via FSP leading to surface strengthening. *Metall. Mater. Trans.* 46 (11), 4813–4818. doi:10.1007/s11661-015-3089-8

Wang, L., Xie, L., Lv, Y., Zhang, L.-C., Chen, L., Meng, Q., et al. (2017). Microstructure evolution and superelastic behavior in Ti-35Nb-2Ta-3Zr alloy processed by friction stir processing. *Acta Mater.* 131, 499–510. doi:10.1016/j.actamat.2017.03.079

Wang, L., Xie, L., Zhang, L.-C., Chen, L., Ding, Z., Lv, Y., et al. (2018a). Microstructure evolution and superelasticity of layer-like NiTiNb porous metal prepared by eutectic reaction. *Acta Mater.* 143, 214–226. doi:10.1016/j.actamat.2017.10.021

Wang, Z.-X., Chen, G.-Q., Chen, L.-Y., Xu, L., and Lu, S. (2018b). Degradation behavior of micro-arc oxidized ZK60 magnesium alloy in a simulated body fluid. *Metals* 8 (9), 724. doi:10.3390/met8090724

Xiang, K., Chen, L.-Y., Chai, L., Guo, N., and Wang, H. (2020). Microstructural characteristics and properties of CoCrFeNiNbx high-entropy alloy coatings on pure titanium substrate by pulsed laser cladding. *Appl. Surf. Sci.* 517, 146214. doi:10.1016/j.apsusc.2020.146214

Yang, H.-Y., Wang, Z., Shu, S.-L., and Lu, J.-B. (2020a). Effect of Ta addition on the microstructures and mechanical properties of in situ bi-phase (TiB2-TiCxNy)/(Ni-Ta) cermets. *Ceram. Int.* 45 (4), 4408–4417. doi:10.1016/j.ceramint.2018.11.118

Yang, H.-Y., Wang, Z., Yue, X., Ji, P.-J., and Shu, S.-L. (2020b). Simultaneously improved strength and toughness of in situ bi-phased TiB2–Ti(C,N)–Ni cermets by Mo addition. *J. Alloys Compd.* 820, 153068. doi:10.1016/j.jallcom.2019.153068

Yang, H., Yue, X., Wang, Z., Shao, Y., and Shu, S. (2020c). Strengthening mechanism of TiC/Al composites using Al-Ti-C/CNTs with doping alloying elements (Mg, Zn and Cu). *J. Mater. Res. Tech.* 9 (3), 6475–6487. doi:10.1016/j.jmrt.2020.04.033

Yang, Y., Chen, Y., Zhang, J., Gu, X., Qin, P., Dai, N., et al. (2018). Improved corrosion behavior of ultrafine-grained eutectic Al-12Si alloy produced by selective laser melting. *Mater. Des.* 146, 239–248. doi:10.1016/j.matdes.2018.03.025

Yang, Z. N., Wang, X. B., Liu, F., Zhang, F. C., Chai, L. J., Qiu, R. S., et al. (2019). Effect of intercritical annealing temperature on microstructure and mechanical properties of duplex Zr-2.5Nb alloy. *J. Alloys Compd.* 776, 242–249. doi:10.1016/j.jallcom.2018.10.320

Yu, F., Addison, O., and Davenport, A. J. (2015). A synergistic effect of albumin and H_2O_2 accelerates corrosion of Ti_6Al_4V. *Acta Biomater.* 26, 355–365. doi:10.1016/j.actbio.2015.07.046

Zhang, B., Wang, J., Wu, B., Guo, X. W., Wang, Y. J., Chen, D., et al. (2018). Unmasking chloride attack on the passive film of metals. *Nat. Commun.* 9 (1), 2559. doi:10.1038/s41467-018-04942-x

Zhang, H., Man, C., Wang, L., Dong, C., Wang, L., Kong, D., et al. (2020a). Different corrosion behaviors between α and β phases of Ti6Al4V in fluoride-containing solutions: influence of alloying element Al. *Corrosion Sci.* 169, 108605. doi:10.1016/j.corsci.2020.108605

Zhang, L.-C., and Attar, H. (2016). Selective laser melting of titanium alloys and titanium matrix composites for biomedical applications: a review. *Adv. Eng. Mater.* 18 (4), 463–475. doi:10.1002/adem.201500419

Zhang, L.-C., Chen, L.-Y., and Wang, L. (2020b). Surface modification of titanium and titanium alloys: technologies, developments and future interests. *Adv. Eng. Mater.* 22 (5), 1901258. doi:10.1002/adem.201901258

Zhang, L.-C., Xu, J., and Eckert, J. (2006). Thermal stability and crystallization kinetics of mechanically alloyed TiC/Ti-based metallic glass matrix composite. *J. Appl. Phys.* 100 (3), 033514. doi:10.1063/1.2234535

Zhang, L. C., and Chen, L. Y. (2019). A review on biomedical titanium alloys: recent progress and prospect. *Adv. Eng. Mater.* 21 (4), 1801215. doi:10.1002/adem.201801215

Zhang, L., Chen, L.-Y., Zhao, C., Liu, Y., and Zhang, L.-C. (2019a). Calculation of oxygen diffusion coefficients in oxide films formed on low-temperature annealed Zr alloys and their related corrosion behavior. *Metals* 9 (8), 850. doi:10.3390/met9080850

Zhang, L. C., Jia, Z., Lyu, F., Liang, S. X., and Lu, J. (2019b). A review of catalytic performance of metallic glasses in wastewater treatment: recent progress and prospects. *Prog. Mater. Sci.* 105, 100576. doi:10.1016/j.pmatsci.2019.100576

Zhang, L. C., Klemm, D., Eckert, J., Hao, Y. L., and Sercombe, T. B. (2011). Manufacture by selective laser melting and mechanical behavior of a biomedical Ti-24Nb-4Zr-8Sn alloy. *Scripta Mater.* 65 (1), 21–24. doi:10.1016/j.scriptamat.2011.03.024

Zhang, L. C., Shen, Z. Q., and Xu, J. (2003). Glass formation in a (Ti, Zr, Hf)–(Cu, Ni, Ag)–Al high-order alloy system by mechanical alloying. *J. Mater. Res.* 18 (9), 2141–2149. doi:10.1557/jmr.2003.0300

Zhang, L. C., and Xu, J. (2004). Glass-forming ability of melt-spun multicomponent (Ti, Zr, Hf)–(Cu, Ni, Co)–Al alloys with equiatomic substitution. *J. Non-cryst. Solids* 347 (1–3), 166–172. doi:10.1016/j.jnoncrysol.2004.09.007

Zhang, M., Li, Y. N., Zhang, F. C., Wang, X. B., Chen, L. Y., and Yang, Z. N. (2017). Effect of annealing treatment on the microstructure and mechanical properties of a duplex Zr-2.5 Nb alloy. *Mater. Sci. Eng. A* 706, 236–241. doi:10.1016/j.msea.2017.08.107

Zhang, Y.-M., Chen, L.-Y., Lu, S., Zhao, C., and Wang, Y.-H. (2019c). Refined microstructure and enhanced hardness in friction stir-welded AZ31 magnesium alloy induced by heat pipe with different cooling liquid. *Metals* 9 (11), 1227. doi:10.3390/met9111227

Zhao, S., Li, S. J., Wang, S. G., Hou, W. T., Li, Y., Zhang, L. C., et al. (2018). Compressive and fatigue behavior of functionally graded Ti-6Al-4V meshes fabricated by electron beam melting. *Acta Mater.* 150, 1–15. doi:10.1016/j.actamat.2018.02.060

Zheng, X., Gong, M., Xiong, T., Ge, H., Yang, L., Zhou, Y., et al. (2019). Deformation induced FCC lamellae and their interaction in commercial pure Ti. *Scripta Mater.* 162, 326–330. doi:10.1016/j.scriptamat.2018.11.037

Conflict of Interest: The authors declare that the research was conducted in the absence of any commercial or financial relationships that could be construed as a potential conflict of interest.

Copyright © 2021 Yi, Liu, Zheng, Zhang, Xu, Cui and Liu. This is an open-access article distributed under the terms of the Creative Commons Attribution License (CC BY). The use, distribution or reproduction in other forums is permitted, provided the original author(s) and the copyright owner(s) are credited and that the original publication in this journal is cited, in accordance with accepted academic practice. No use, distribution or reproduction is permitted which does not comply with these terms.